A multifield loads evaluation method for offshore wind turbines considering multivariate coherence effect

Kai Xu[a], Fushun Liu[a,b,*], Dianzi Liu[a,c]

[a]*College of Engineering, Ocean University of China, Qingdao 266100 , China*
[b]*Shandong Province Key Laboratory of Ocean Engineering, Ocean University of China, Qingdao 266100, China*
[c]*School of Engineering, University of East Anglia, Norwich, NR14 7TH, United Kingdom*

Abstract

The structural design and reliability assessment of offshore wind turbine systems for maximally exploring the renewable energy resources significantly rely on the actual marine environmental loads. The major challenges arising from the estimation of offshore wind turbine loads are the effects of rotating blades on wind velocity and the interactions among multiple components such as wind, waves and the structure. These factors make the environmental loads more complex and multivariately correlated. To address such issues, a multivariate coherence effect (MCE)-based evaluation method has been proposed to analyze the rotational effect on the wind velocity by discovering the perturbation mechanism of wind spectrum. Furthermore, analytical formulations in the form of the blade speed and wind spectrum have been developed to construct the MCE-based joint power spectrum matrix for the load redistribution via intercorrelations among multiple domains representing the ambient environment of offshore wind turbines. Results show that the MCE-based method has the ability to retain the characteristic multiple rotational frequencies of rotational blades and enables the simultaneous reconstructions of the stationary-state wind field, rotational wind field and wave height sequences for accurate load redistributions by decomposing the MCE-based joint power spectrum matrix. As compared with the traditional techniques, a more cost-effective approach can be further developed for the reliable estimation of the blade flapwise deflection using the proposed method. Summarily, the present work provides analytical formations for the accurate load configuration and dynamic analysis of offshore wind turbines subject to harsh marine environments.

Keywords:
Rotational effect spectrum; Multivariate coherence effect; Load redistribution; Offshore wind turbine

1. Introduction

As a family of infrastructures supporting green energy exploitation, offshore wind turbine (OWT) structures have received increasing attention in marine engineering due to their capability to generate renewable wind energy (Lian et al., 2021, Liu et al., 2019, Zhang et al., 2016). At present, 80% of the worlds offshore wind resources are located in water deeper than 60 meters. In order to leverage the power of the rich wind energy, major developed countries have

*Corresponding author.
Email address: percyliu@ouc.edu.cn (Fushun Liu)

Nomenclature

a	Attenuation coefficient	L_{op}^{bt}	Coherence distance between rotational and stationary-state wind speeds
A_n	Coefficient of the Fourier series expansion	L_{pq}^{ww}	Coherence distance between stationary -state wind speeds and waves
A_w	Effective windward area	$L_{oq}^{ww\prime}$	Coherence distance between rotational wind speeds and waves
$APSD$	Auto power spectral density	MCE	Multivariate coherence effect
BEM	Blade element momentum	N	Number of discrete frequencies
c	Chord length of the blade	r	Distance from the point of simulated wind speed to the hub
C_d, C_l	Drag and lift coefficients of the airfoil	R_{ij}	Cross-correlation function of stationary-state wind speeds
C_D, C_M	Drag and mass coefficients of the wave	$\tilde{R}_{ij}$	Cross-correlation function of rotational wind speed
C_N	Normal coefficient of the blade element	RES	Rotational effect spectrum
Coh^{bb}	Coherence function of rotational wind speeds	$\tilde{S}_{ij}^{bb}$	CPSD of rotational wind speeds
Coh^{bt}	Coherence function between rotational and stationary-state wind speeds	$\tilde{S}_{op}^{bt}$	CPSD between rotational and stationary -state wind speeds
Coh^{ww}	Coherence function between stationary -state wind speeds and waves	$\tilde{S}_{pq}^{ww}$	CPSD between stationary-state wind speeds and waves
$\mathrm{Coh}^{ww\prime}$	Coherence function between rotational wind speeds and waves	$\tilde{S}_{oq}^{ww\prime}$	CPSD between rotational wind speeds and waves
$CPSD$	Cross power spectral density	S^w	JONSWAP spectrum
f	Frequency	S_{karman}	Karman spectrum
f_0	Blade rotational frequency	T_p	Period of the wave
f_g	Gravity load of the blade	u_b	Wind speed on the blade
F_{flap}	Generalized aerodynamic load	u_t	Wind speed on the tower
$H_{q\times q}$	MCE-based joint spectrum matrix	$\dot{u_f}, u_f$	Acceleration and velocity of the fluid particle
H_s	Significant wave height	ϕ	Initial phase angle of the blade
L_c	Integral length scale	ϕ_0	Blade distribution angle
L_{ij}^{bb}	Coherence distance of rotational wind speeds	θ	Delay parameter
		w_N	Upper cut-off frequency

shifted their research focus to the area related to the deeper sea (Ferčák et al., 2022, Zountouridou et al., 2015). With the development of large-scale and high-power wind turbines, the blade of wind turbines presents the features of the large slenderness ratio and flexibility, which lead to a more pronounced rotational effect on structural performances of wind power structures (Murtagh et al., 2005). Moreover, the wind and wave coherence effects should be considered in the calculation of wind loads as the interaction between wind and wave becomes more evidently in the complex deeper sea environment.

Reviews on wind loads initially focused on land-based fixed tower structures, and later wind spectrum that can meet the design need of offshore floating structures emerged along with the available data of offshore turbulent wind (Damgaard et al., 2013, Davenport, 1962, Simiu, 1974). Unlike the wind loads in the stationary tower, the rotation of the offshore wind turbine blades causes a redistribution of energy in the wind spectrum. Thus, the perturbations generated by the rotational effect have a significant impact on the behaviors of wind profiles across the rotating region. To consider the rotational effect of blades, the time domain model developed in the FAST and Blade software was proposed by the Sandia National Laboratories (SNL) (Moriarty and Hansen, 2005) and a discrete sampling pattern was used as the blades moved. Then, the rotating region was sequentially sampled to obtain the rotating wind speed, leading to data discontinuities. As compared with the proposed SNL method, the rotational sampling of wind speeds was replaced by the updated eigenmodes of the blade using B-sample surface interpolation to ensure the accuracy in evaluating turbulent wind speeds (Chen et al., 2015). Although considerable efforts have been contributed to improve the capability of algorithms in dealing with the rotational effects on wind loads in time-domain analysis methods, the wind spectrum has been intrinsically defined in a traditional form and the problem of discontinuities due to the discrete sampling has remained unresolved. Also, Ris National Laboratory (RNL) established a time domain model based on the filter composition (Hansen et al., 2002, Sørensen et al., 2002). Its assumption lay in the fact that the wind turbine was a low power filter and this reduced the effect of higher order harmonics on the rotor. This method does not consider the analytical expression of the wind spectrum and the correlation analysis could not be performed due to the asymmetry of the wind spectrum. Meanwhile, based on the RNL model, other nonparametric frequency models for rotationally sampled turbulent winds was developed using a filter synthesis method (Burlibaşa and Ceangă, 2013). However, the common feature in these models is a time-domain approach that does not describe the rotational effect of blades in terms of physical mechanisms.

The frequency domain approach for describing the rotational effect of the blade was initially enhanced by establishing the relationship between the auto-correlation and cross-correlation functions (Connell, 1982). However, the analytical representation of the wind spectrum limited its application. Based on this approach, the analytical form of the rotational wind spectrum was developed and simpler explicit expressions were derived (Chen et al., 2020, Tian et al., 2012). Murtagh et al. (2004) derived the coefficients of discrete Fourier transform and determined the specific frequency of rotational blades to facilitate the desired spectral energy redistribution. Despite the preceding advance in modeling the rotational sampling from the frequency domain, these methods only considered the single coherent effect (Højstrup, 1999, Tian et al., 2012, Vigueras-Rodríguez et al., 2012). That is to say, only the coherence at the blade rotation level was described, and the coherence effects among rotational, stationary, and wind-wave associated regions were not considered. Besides, the segmented simulation approach tended to lead to non-simultaneous load-

ings of the marine environment (Ji et al., 2011, Karimirad and Moan, 2012). In order to realistically explore wind loads in complex marine environments, the MCE of actual wind loads should be considered.

Typically, the offshore wind turbine under operation divided the entire wind field area into rotating and non-rotating regions (Banerjee et al., 2019, Feyzollahzadeh et al., 2016, Tian et al., 2012). The wind loads needed to be considered separately for the region itself and for the inter-region. More specifically, the coherence of wind speeds in the rotating region itself was found at different locations on the same blade and on different blades, while the coherence of wind speeds between blades and the tower was noted across the rotating and non-rotating regions. Furthermore, a correlation between wind and waves depending on the rough length of the air was found (Johnson et al., 1998, Wu, 1969). The atmosphere acted on the wave surface in the form of wind stress to provide kinetic energy, and in turn, the wave surface acted on the atmosphere through heat transfer and evaporation (Kudryavtsev et al., 1999). Therefore, the study of the spatial correlation between wind and wave fields needs to consider the coupling mechanism of wind and waves. Amini et al. (2021) proposed an uncertainty-aware scheme to model uncertainty quantification. In the developed approach, the copula function was introduced to capture the nonlinear dependency between uncertain parameters in the failure probability estimation of infrastructures. Group (1988) used wind as an input for the third generation wave model to describe the fundamental transport equation for the evolution of the two-dimensional wave spectrum. Elsayed (2006) employed wavelet bicoherence to analyze wind and waves data measured simultaneously during Mistral, pointing out that the phase coupling occurs between wind speed and wave height in a certain frequency range. More recently, He (2020) calculated the average power spectral density and coherence function of the wind speed and wave height based on the wind and wave information in the FETCH experiment. The accurate assessment of the combination of wind and wave forces is prerequisite information for analysing the complex coupled vibration characteristics of offshore wind turbines (Ding et al., 2023). Colwell and Basu (2009) accurately formulated the correlated wind and wave loads of offshore wind turbines by combining Kaimal spectrum with JONSWAP wave spectrum. Also, the correlation of significant wave height and peak periods with the wind speed was uesd to construct environmental loads for floating vertical axis wind turbines (Cheng et al., 2016). Furthermore, the dependence structure of multiple wind and wave-related environmental parameters was developed to determine the long-term design loads of the spar type FOWT (Li and Zhang, 2020). In these methods, the rotational spectrum has been rarely considered to assess aerodynamic loads on the blade, and wind and waves have been simply correlated through parameters such as wave height, peak period and wind speed. Moreover, to our best knowledge, there have been almost no MCE load analysis methods that consider the integration of the rotational, stationary, and wind wave domains. Therefore, it is crucial to develop a new MCE analysis method that consider the rotational effect for offshore wind turbines.

In this paper, a novel MCE-based RES method has been proposed to evaluate the rotational effect and enable the coupling analysis of multifield spectrums. Furthermore, the accurate multifield loads on offshore wind turbines have been achieved by constructing a MCE-based joint power spectrum matrix. This paper has been organized as follows: Section 2 has provided a detailed mathematical description of the underlying theory of wind loads along with a discussion of its limitations. In Section 3, the theoretical derivation of the RES has been carried out and the MCE mechanism has been introduced. In Section 4, the correctness of the proposed method has been demonstrated

throughout the examples. Finally, the potential research on the wind rotational effect using the proposed MCE-based approach has been summarized in Section 5.

2. Preliminaries

2.1. Taylor's frozen turbulence hypothesis

Taylor's frozen turbulence hypothesis lies in that the change in the turbulence velocity u at the fixed point is caused by the passage of an unchanging pattern for the turbulent motion at the point. Assume that the turbulent velocity at the position l_0 at time t is $u(l_0, t)$, thus the turbulent velocity $u(l_0 + \Delta l_0, t + \tau)$ at time $t + \tau$ at the downstream $l_0 + \Delta l_0$ can be approximated by the following equation:

$$u(l_0 + \Delta l_0, t + \tau) = u(l_0 + \Delta l_0 - U_0\tau, t) \tag{1}$$

where U_0 is the mean turbulence velocity.

Based on the above assumption, the wind speed at different moments on the blade can be equated with the wind speed at different locations for the same time. The similar equations for the cross-correlation function can also be derived.

2.2. Harmonic superposition principle

The time series of the wind speed can be written in the form of a linear superposition of trigonometric functions based on the decomposition of the wind spectrum matrix (Hao et al., 1989),

$$u_j(t) = \sum_{m=1}^{j} \sum_{g=1}^{N} A_{jm}(\omega_g) \cos\left[\omega_g t + \beta_{jm}(\omega_g) + \varphi_{mg}(\omega_g)\right] \quad j = 1, 2, \ldots, q \tag{2}$$

where ω_g is the gth frequency; A_{jm} is the amplitude at the frequency ω_g and β_{jm} denotes the corresponding phase angle; φ_{mg} represents the random phase angle uniformly distributed over the range of 0 to 2π ; q denotes the qth of wind speed point and N means the number of discrete frequencies, respectively.

As it is quite time consuming to generate wind speed data using Eq. 2, wind speed time histories are more efficiently constructed in the frequency domain using Fast Fourier Transform technique (Bi and Hao, 2012, Shinozuka and Deodatis, 1991). When the fluctuating wind speed series are generated by the harmonic superposition principle, two key aspects should be considered as follows:

• Decomposition anomalies caused by the Non-Hermite positive definite matrix in the decomposition of the joint power spectrum matrix.

• The construction efficiency of wind speed series using Fast Fourier transform technique.

2.3. Blade element momentum

The blade element momentum (BEM) theory is the combination of both the blade element theory and momentum theory. The steady state load, thrust and power of the offshore wind turbine subject to different wind-speed loadings,

the blade speed and pitch angle can be calculated using BEM. The lift force P_L and drag force P_D applied to the blade element unit can be expressed as:

$$\begin{cases} P_L = \frac{1}{2}\rho V_{rel}^2 c C_l \\ P_D = \frac{1}{2}\rho V_{rel}^2 c C_d \end{cases} \tag{3}$$

where V_{rel} is the relative velocity of the blade element in a function of both the wind speed and the blade velocity; ρ is the air density; c is the chord length of the blade element; C_l and C_d are the lift and drag coefficients of the airfoil, respectively.

To obtain accurate aerodynamic loads, the BEM theory is substantially improved by two practical considerations:

• The assumption of the infinite number of blades is corrected by the Planter′s tip loss factor to ensure the accuracy of the aerodynamic loads as the airflow sweeps over the tip of the blade.

• The Momentum theory is modified to avoid the stall of wind turbine blades when the axial induction factor is approximately greater than 0.4.

3. Multivariate coherence-based rotational effects spectrum

The basic idea of the RES is that the wind speed on rotating blades is described in the form of a spectrum, which contains a combination of factors such as the blade speed, spatial position and fluctuating wind spectrum. Unlike the rotational sampling method in the time domain, the explicit analytical form of RES defined by the correlation function in the frequency domain has its spectral representation.

3.1. Rotational effect wind spectrum

Assume that the wind speed at the time t and $t+\tau$ are depicted as $v_i(t)$ and $v_j(t+\tau)$, respectively. The Fourier transform of the time series for the wind speed can be expressed as:

$$\begin{cases} \mathcal{F}_i(f) = \int_0^T v_i(t) \cdot e^{-I_m 2\pi f t} dt \\ \mathcal{F}_j(f) = \int_0^T v_j(t+\tau) \cdot e^{-I_m 2\pi f (t+\tau)} d(t+\tau) \end{cases} \tag{4}$$

where $\mathcal{F}_i(f)$ and $\mathcal{F}_j(f)$ are obtained by the Fourier transform of time series of wind speeds $v_i(t)$ and $v_j(t+\tau)$ at the time of t and $t+\tau$, respectively. $I_m = \sqrt{-1}$ denotes the imaginary unit and f is the discrete frequency .

The power spectral density $\mathcal{F}_{si}(f)$, $\mathcal{F}_{sj}(f)$ of time series from blades can be defined as:

$$\begin{cases} \mathcal{F}_{si}(f) = \frac{1}{\sqrt{T}} \int_0^T v_i(t) \cdot e^{-I_m 2\pi f t} dt \\ \mathcal{F}_{sj}(f) = \frac{1}{\sqrt{T}} \int_0^T v_j(t+\tau) \cdot e^{-I_m 2\pi f (t+\tau)} d(t+\tau) \end{cases} \tag{5}$$

Subsequently, the cross-correlation function $R_{ij}(\tau)$ between time series $v_i(t)$ and $v_j(t+\tau)$ can be written as:

$$R_{ij}(\tau) = \frac{1}{T} \int_0^T v_i(t) v_j(t+\tau) \mathrm{d}t \tag{6}$$

Substituting Eq. (4) into Eq. (6), one has:

$$R_{ij}(\tau) = \frac{1}{T} \int_0^T \mathcal{F}_j(f) e^{\mathrm{I_m} 2\pi f \tau} \mathrm{d}f \int_0^T v_i(t) e^{\mathrm{I_m} 2\pi f t} \, \mathrm{d}t \tag{7}$$

Based on the copula principle of the exponential function, the equivalent form associated with $v_i(t)$ can be expressed as:

$$v_i(t)e^{\mathrm{I_m}2\pi ft} = \overline{v_i(t)e^{-\mathrm{I_m}2\pi ft}} \tag{8}$$

Substituting Eq. (8) into equation Eq. (7), the cross-correlation function $R_{ij}(\tau)$ can be further simplified as:

$$\begin{aligned} R_{ij}(\tau) &= \int_0^T \overline{\mathcal{F}_{si}(f)}\mathcal{F}_{sj}(f)e^{\mathrm{I_m}2\pi f\tau}\mathrm{d}f \\ &= \int_0^T \mathcal{F}_{sij}(f)e^{\mathrm{I_m}2\pi f\tau}\mathrm{d}f \end{aligned} \tag{9}$$

where $\overline{\mathcal{F}_{si}(f)}$ is the conjugate form of the power spectral density $\mathcal{F}_{si}(f)$; $\mathcal{F}_{sij}(f)$ is the cross-power spectral density (CPSD) of $v_i(t)$ and $v_j(t+\tau)$.

Assume that the coherence function is denoted as $\mathrm{Coh}(i,j;f)$, the CPSD can be reformulated as follows:

$$\mathcal{F}_{sij}(f) = \sqrt{\mathcal{F}_{si}(f)\mathcal{F}_{sj}(f)}\,\mathrm{Coh}(i,j;f) \tag{10}$$

Therefore, the transformation relationship between the cross-correlation function and the CPSD is established by substituting Eq. (10) into Eq. (9), one has:

$$R_{ij}(\tau) = \int_0^T \sqrt{\mathcal{F}_{si}(f)\mathcal{F}_{sj}(f)}\,\mathrm{Coh}(i,j;f)e^{\mathrm{I_m}2\pi f\tau}\mathrm{d}f \tag{11}$$

Inspired by Eq. (11), two transformation pairs reflecting the relationships between the CPSD of the fluctuating wind spectrum $S_{ij}(f)$ and the cross-correlation function of the stationary-state wind $R_{ij}(\tau)$, and the CPSD of RES $\tilde{S}_{ij}^{bb}(f)$ and the cross-correlation function of the rotational wind $\tilde{R}_{ij}(\tau)$ can be defined by Eq. (12).

$$\begin{cases} R_{ij}(\tau) = \int_{-\infty}^{+\infty} S_{ij}(f)\cdot e^{I_m 2\pi f\tau}df \\ S_{ij}(f) = \int_{-\infty}^{+\infty} R_{ij}(\tau)\cdot e^{-I_m 2\pi f\tau}d\tau \\ \tilde{R}_{ij}(\tau) = \int_{-\infty}^{+\infty} \tilde{S}_{ij}^{bb}(f)\cdot e^{I_m 2\pi f\tau}df \\ \tilde{S}_{ij}^{bb}(f) = \int_{-\infty}^{+\infty} \tilde{R}_{ij}(\tau)\cdot e^{-I_m 2\pi f\tau}d\tau \end{cases} \tag{12}$$

Based on Taylor's frozen turbulence hypothesis, it is concluded that the cross-correlation functions of $\tilde{R}_{ij}(\tau)$ and $R_{ij}(\tau)$ are equal to each other. As the CPSD of the fluctuating wind between Points i and j can be formulated as Eq. (13), the RES in Eq. (12) can be defined by Eq. (14):

$$S_{ij}(f) = \mathrm{Coh}(i,j;f)\sqrt{S_{ii}(f)S_{jj}(f)}e^{-I_m\theta_{ij}(f)} \tag{13}$$

$$\begin{aligned} \tilde{S}_{ij}^{bb}(f) &= \int_{-\infty}^{+\infty} \tilde{R}_{ij}(\tau)\cdot e^{-I_m 2\pi f\tau}d\tau \\ &= \int_{-\infty}^{+\infty}\int_{-\infty}^{+\infty} \sqrt{S_{ii}(f')S_{jj}(f')}Coh\,(i,j;f')\,e^{-I_m\theta_{ij}(f')}df'\cdot e^{-I_m 2\pi(f-f')\tau}d\tau \end{aligned} \tag{14}$$

where $S_{ii}(f)$ and $S_{jj}(f)$ are the auto-power spectrum density (APSD) at Points i and j, respectively. θ_{ij} is the delay parameter between Points i and j.

As the rotational frequency of blades is f_0, the coherence function can be expressed in a function of f_0 and the expansion coefficient A_n by Eq. (15):

$$\begin{cases} \mathrm{Coh}(i,j;f) = \sum_{n=-\infty}^{+\infty} A_n(i,j;f) \cdot e^{I_m n(2\pi f_0 \tau + \phi_0)} \\ A_n(i,j;f) = f_0 \int_0^{1/f_0} \mathrm{Coh}(i,j;f) e^{-I_m n(2\pi f_0 \tau + \phi_0)} d\tau \end{cases} \tag{15}$$

where $A_n(i,j;f)$ is the coefficient of the Fourier series expansion; ϕ_0 represents the blade distribution angle and its value is $2\pi/3$ for the three-blade wind turbine.

Substituting Eq. (15) into Eq. (14), one has:

$$\tilde{S}_{ij}^{bb}(f) = \int_{-\infty}^{+\infty} \sum_{n=-\infty}^{+\infty} \sqrt{S_{ii}(f')S_{jj}(f')} A_n(i,j;f') e^{I_m(n\phi_b - \theta_{ij}(f'))} \int_{-\infty}^{+\infty} e^{-I_m 2\pi(f-f'-nf_0)\tau} d\tau df' \tag{16}$$

As the unique frequency-shift δ_{shift} and sampling δ_{sample} properties of the δ function can be denoted as:

$$\begin{cases} \int_{-\infty}^{+\infty} e^{-I_m 2\pi f \tau} \mathrm{d}\tau = \delta(f) & ,\delta_{shift} \\ \int_{-\infty}^{+\infty} x(f')\delta(f'-f_0)\,\mathrm{d}t = x(f_0) & ,\delta_{sample} \end{cases} \tag{17}$$

where the Dirac δ is defined as:

$$\delta(t) = \begin{cases} +\infty & ,t=0 \\ 0 & ,t \neq 0 \end{cases} \tag{18}$$

The RES $\tilde{S}_{ij}^{bb}(f)$ can be obtained by substituting δ_{shift} defined in Eq. (17) into equation Eq. (16):

$$\tilde{S}_{ij}^{bb}(f) = \int_{-\infty}^{+\infty} \sum_{n=-\infty}^{+\infty} \sqrt{S_{ii}(f')S_{jj}(f')} A_n(i,j;f') e^{I_m(n\phi_b - \theta_{ij}(f'))} \delta(f-f'-nf_0) d\tau df' \tag{19}$$

Similarly, substituting δ_{sample} into Eq. (19), $\tilde{S}_{ij}^{bb}(f)$ can be further expressed as:

$$\tilde{S}_{ij}^{bb}(f) = \sum_{n=-\infty}^{+\infty} \underbrace{A_n(i,j;f-nf_0) \cdot \sqrt{S_{ii}(f-nf_0) S_{jj}(f-nf_0)} \cdot e^{-I_m(\theta(f-nf_0) - n\phi_0)}}_{\textit{Rotational effect mode} \qquad \textit{Source spectrum translation effect} \qquad \textit{Phase delay}} \tag{20}$$

Eq. (20) reveals that the formulation of the derived RES is composed of three parts: the rotational effect mode $A_n(i,j;f-nf_0)$, the source spectrum translation effect in a form of $S(f-nf_0)$ and the phase delay $e^{-I_m(\theta(f-nf_0)-n\phi_0)}$. It is worth noting that as the amplitude of the source spectrum translation effect is attenuated by both a local minimum of the rotational mode and the phase delay, the oscillatory attenuation of RES can be observed.

When $\theta(f-nf_0)$ is equal to zero, the RES can be further simplified by substituting Eq. (15) into Eq. (20):

$$\tilde{S}_{ij}^{bb}(f) = \begin{cases} \sum_{n=-\infty}^{+\infty} f_0 \int_0^{1/f_0} Coh(i,j;f)\, e^{-I_m n(2\pi f_0 \tau)} d\tau \sqrt{S_{ii}(f-nf_0) S_{jj}(f-nf_0)} & ,i \neq j \\ \sum_{n=-\infty}^{+\infty} f_0 \int_0^{1/f_0} Coh(i,j;f)'\, e^{-I_m n(2\pi f_0 \tau)} d\tau S_{ii}(f-nf_0) & ,i=j \end{cases} \tag{21}$$

When $\phi_0 \neq 0$ is given in Eq. (21), the rotational effect is reflected by the CPSD on different blades. Similarly, when $i=j$ and the phase factor $\phi_0 = 0$ are satisfied, the rotational effect is dominated by the APSD on the same blade.

Letting $\vartheta = 2\pi f_0 \tau$, the RES can be rewritten as :

$$\tilde{S}_{ij}^{bb}(f) = \begin{cases} \frac{1}{2\pi}\sum_{n=-\infty}^{+\infty}\int_0^{2\pi} Coh\left(\vartheta, f-nf_0\right)\cos(n\vartheta)d\vartheta \cdot \sqrt{S_{ii}(f-nf_0)S_{jj}(f-nf_0)} & ,i \neq j \\ \frac{1}{2\pi}\sum_{n=-\infty}^{+\infty}\int_0^{2\pi} Coh\left(\vartheta, f-nf_0\right)'\cos(n\vartheta)d\vartheta \cdot S_{ii}\left(f-nf_0\right) & ,i = j \end{cases} \tag{22}$$

It can be observed that the solution in Eq. (22) is susceptible to divergence by oscillatory integrals. Therefore, the Gauss-Lejeune integral method is employed to solve the integral convergence problem. It is described as follows:

• The integration interval $[\vartheta_a, \vartheta_b]$ is mapped to the standard interval $t_j \in [\ 1,1]$ by the variable transformation $\vartheta = \frac{\vartheta_b - \vartheta_a}{2} t_j + \frac{\vartheta_a + \vartheta_b}{2}$.

• The corresponding Gauss-Lejeune integral formula is approximated by a summation of functions represented by Gaussian coefficients and the transformed variable:

$$\int_{\vartheta_a}^{\vartheta_b} f(\vartheta)d\vartheta \approx \frac{\vartheta_b - \vartheta_a}{2}\sum_{j=1}^{n_j} A_j f\left(\frac{\vartheta_b - \vartheta_a}{2}t_j + \frac{\vartheta_a + \vartheta_b}{2}\right) \tag{23}$$

where t_j is the Gaussian point and A_j is the Gaussian coefficient.

3.2. MCE-assisted domain partitioning

The MCE considers the combination of the rotational wind loads on the blades, stationary-state wind loads on the tower and wave loads. Therefore, it represents a complex correlation, which is mainly constituted by coupled spectrum matrixes. Typically, the entire coherence domain for performance analysis of the offshore wind turbine is divided into four parts including the rotational coherence domain (Domain I), rotational and stationary-state coherence domain (Domain II), stationary-state and wave coherence domain (Domain III), and rotational and wave coherence domain (Domain IV), as shown in Fig. 1. To achieve simultaneous correlation of multifield loads with a high level of accuracy, the MCE-assisted rotational wind load reconstruction method based on the principle of domain partitioning has been proposed in this study.

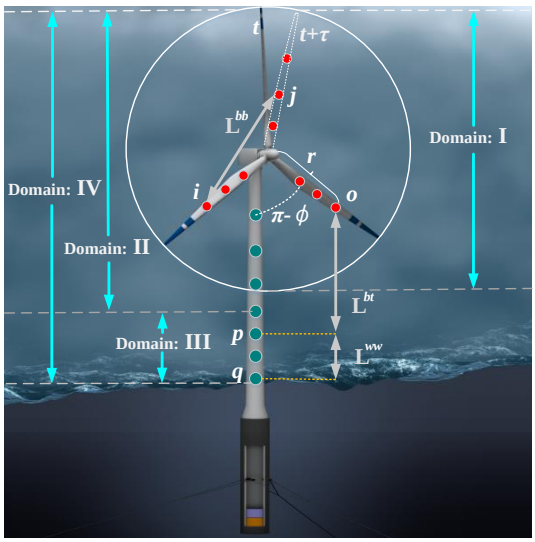

Fig. 1: The schematic of coherent domain partitioning.

Domain I: Coherence between rotational wind speeds

As described in Eq. (20), the oscillatory attenuation of the RES $\tilde{S}_{ij}^{bb}(f)$ has been influenced by three components, especially the rotational mode. Furthermore, the energy redistribution due to the RES represented by the coherence function has been determined by Eq. (21). Considering the rotational coherence of the different wind speeds in Domain I, the RES has been reformulated to discover energy correlation mechanism as follows:

$$\begin{cases} \tilde{S}_{ij}^{bb}(f) = \sum_{n=-\infty}^{+\infty} f_0 \int_0^{1/f_0} \mathrm{Coh}^{bb}(i,j;f) e^{-I_m n(2\pi f_0 \tau)} d\tau \sqrt{S_{ii}\left(f - nf_0\right) S_{jj}\left(f - nf_0\right)} \\ \mathrm{Coh}^{bb}(i,j;f) = \exp\left[-aL_{ij}^{bb}(\tau)\sqrt{\left(\frac{f}{\bar{U}_{bb}}\right)^2 + \left(\frac{0.12}{L_c}\right)^2}\right] \end{cases} \tag{24}$$

where $Coh^{bb}(i,j;f)$ is the dynamic Davenport coherence function in the rotational domain (Davenport, 1963); L_c depicts the integral length scale; a means the attenuation coefficient; L_{ij}^{bb} represents the dynamic coherence distance. $\bar{U}_{bb}$ denotes the mean wind speed at the midpoint between i and j in the rotational domain and can be further formulated in a power form as follows:

$$\bar{U}_{bb} = \left(\frac{2h_0 + (\mathrm{r_i} + \mathrm{r_j})\cos\left(2\pi f_0 t + \phi\right)}{h_0}\right)^{\alpha} * \bar{U}_{h_0} \tag{25}$$

where r_i and r_j represent the radial distance from the Points i and j to the hub, respectively; $\bar{U}_{h_0}$ denotes the mean wind speed at the reference height h_0; α is the surface roughness coefficient and h is the blade height.

As the dynamic coherence distance L_{ij}^{bb} under different wind speeds varies with the blade frequency, it can be defined by Eq. (26):

$$L_{ij}^{bb} = \begin{cases} \{2r_i \left|\sin\left(\pi f_0 \tau\right)\right| & , B_1 \to B_1 \\ \sqrt{r_i^2 + r_j^2 - 2r_i r_j \cos\left(2\pi f_0 \tau + \phi\right)} & , B_1 \to B_2 \end{cases} \tag{26}$$

where $B_1 \to B_1$ and $B_1 \to B_2$ depict two points on the same and different blades, respectively.

Domain II: Coherence between rotational and stationary-state wind speeds

In this domain, the coherence between wind speeds along the blades and the tower has been established based on the principle of dynamic transformation considering the correlation of dynamic and stationary-state domains. More specifically, the wind speeds in the rotating coordinate system have been converted to the stationary-state wind speeds in the static coordinate system by the RES. Thus, the CPSD between the wind speeds at Points o (on the blade) and p (on the tower) in Fig. 1 can be expressed in a combination of both the RES and stationary-state coherence function as:

$$\tilde{S}_{op}^{bt}(f) = \mathrm{Coh}^{bt}(o,p;f)\sqrt{\tilde{S}_{oo}^{bb}(f) S_{pp}^{t}(f)} e^{-I_m \theta_{op}} \tag{27}$$

where $S_{pp}^{t}(f)$ is the fluctuating wind spectrum at Point p on the tower. $\mathrm{Coh}^{bt}(o,p;f)$ is the coherence function of wind speeds between Points o and p. Based on Eq. (24), the coherence function $\mathrm{Coh}^{bt}(o,p;f)$ can be obtained in the form of Eq. (28):

$$\mathrm{Coh}^{bt}(o,p;f) = \exp\left[-aL_{op}^{bt}\sqrt{\left(\frac{f}{\bar{U}_{bt}}\right)^2 + \left(\frac{0.12}{L_c}\right)^2}\right] \tag{28}$$

where $L_{op}^{bt} = r_o \cos(\phi) + L^{th}$ means the coherence distance between Points o and p; r_o represents the radial distance from the Point o to the hub and ϕ_o denotes the initial phase angle at Point o on the blade in Fig. 1; L^{th} is the vertical distance from the tower to the hub. $\bar{U}_{bt}$ means the mean wind speed at the midpoint between o and p; If the midpoint locates in the rotational domain, $\bar{U}_{bt}$ is formulated by Eq. (25), otherwise it is defined as follows:

$$\bar{U}_{bt} = \left(\frac{h_o + h_p}{2h_0}\right)^{\alpha} * \bar{U}_{h_0} \tag{29}$$

where h_o and h_p are the heights of Points o and p, respectively.

Domain III: Coherence between stationary-state wind speeds and waves

As the interaction between wind and wave will be inevitably reflected on the foundation of the tubular tower near the sea level, the coherence effect between the stationary-state wind and waves has been evaluated in Domain III. Using Points p and q, located at the tower and sea level respectively, as the reference points, the CPSD between the wave and the stationary-state wind speed is shown in Eq. (30):

$$\tilde{S}_{pq}^{ww}(f) = \mathrm{Coh}^{ww}(p, q; f)\sqrt{S_{pp}^{t}(f) S_{qq}^{w}(f)}e^{-I_m \theta_{pq}} \tag{30}$$

where $\mathrm{Coh}^{ww}(p, q; f)$ is the stationary-state wind and wave coherence function between Points p and q. $S_{qq}^{w}(f)$ is the JONSWAP wave spectrum at Point q on the tower and can be defined as (Goda, 1999):

$$S^{w}(f) = \frac{1}{5} H_s^2 T_p \left(\frac{f}{f_p}\right)^5 \exp\left[-\frac{5}{4}\left(\frac{f}{f_p}\right)^{-4}\right] \gamma^{\exp\left[-\frac{(\omega-\omega p)^2}{2\sigma^2\omega_p^2}\right]} \tag{31}$$

where T_p is the peak spectral period of the wave and $f_p = 1/T_p$; H_s means the significant wave height; σ denotes the peak shape coefficient, σ=0.09 for $f \leqslant f_p$ and σ=0.09 for $f > f_p$. γ represents the JONSWAP peakedness parameter.

It is shown that the spatial coherence of the offshore wind field has been overestimated by the exponential attenuation model of the coherence function for the land wind field due to its stronger spatial coherence. To obtain the accurate coherence model applied to the offshore wind field, the exponential attenuation coefficients for the stationary-state wind and wave coherence models such as the FETCH model and the Frya model have been developed using wind and wave data measured simultaneously (Andersen and Løvseth, 2006, Drennan, 2003, Pettersson, 2003). As the strong wind-wave interactions are included in the complete data set of the FETCH experiment, the coherence function between wind-wave time series at Points p and q as shown in Eq. (32), calculated by regression analysis based on 50 sets of recorded wind and wave data measured simultaneously in the FETCH experiment, has been chosen to study the wind-wave coherence (He, 2020).

$$\mathrm{Coh}^{ww}(p, q; f) = x\left[\frac{fkL_{pq}^{ww}}{\frac{H_s}{T_p} + \bar{U}_p}\right]^{y} \exp\left[-\frac{fkL_{pq}^{ww}}{\frac{H_s}{T_p} + \bar{U}_p}\right] \tag{32}$$

where the parameter x is the scale parameter; k and y denote shape parameters; L_{pq}^{ww} represents the coherence distance from the wave level to the tower; $\bar{U}_p$ means the mean wind speed at Point p.

Domain IV: Coherence between rotational wind speeds and waves

The development of deep-sea floating wind turbines has been accompanied by longer blade structures which result in closer proximity to the sea level. Moreover, the deep sea environment is more prone to be extreme sea conditions due to intense interaction between sea winds and deep water waves. These factors lead to more significant coherence of the wind and waves in the deep-sea environment. Therefore, the coherence of the rotational wind and waves has to be established for the accommodation of load reconstructions in the harsh marine environment. Similarly, the CPSD between the rotational wind and the wave represented by Points o and q has been constructed by combining the dynamic transformation effect and the wind-wave coherence effect in Domain IV by Eq. (33):

$$\begin{cases} \tilde{S}_{ij}^{bb}(f) = \sum_{n=-\infty}^{+\infty} f_0 \int_0^{1/f_0} \mathrm{Coh}^{bb}(i,j;f) e^{-I_m n(2\pi f_0 \tau)} d\tau \sqrt{S_{ii}\left(f - nf_0\right) S_{jj}\left(f - nf_0\right)} \\ \\ \mathrm{Coh}^{ww\prime}(o,q;f) = x \left[\frac{fkL_{oq}^{ww\prime}}{\frac{h_s}{T_p} + \bar{U}_o} \right]^y \exp\left[-\frac{fkL_{oq}^{ww\prime}}{\frac{h_s}{T_p} + \bar{U}_o} \right] \end{cases} \tag{33}$$

where $\mathrm{Coh}^{ww\prime}(o,q;f)$ and $L_{oq}^{ww\prime} = (r_o \cos(\phi) + L^{wh})$ represent the wind-wave coherence function and the coherence distance between the Points o and q, respectively. L^{wh} denotes the coherence distance from the wave level to the hub; $\bar{U}_o$ means the mean wind speed at Point o.

3.3. MCE-based multifield load reconstruction

To improve the computational efficiency in the process of evaluating dynamic responses of structures, the random wind and waves have been modelled independently to reflect their different spectral peak frequencies and frequency distributions (Datta and Jain, 1990). As the correlation between the wind and waves has been ignored, this has led to less accuracy of parameters including the resolution and range of frequencies, the duration of the stationary-state wind and the period of random waves. Therefore, the MCE-based joint spectrum matrix of offshore multifield spectral has been proposed in this work to investigate the correlation between wind and wave for reconstructing their loads on the wind turbine with a high level of accuracy. The correlations of the domains shown in Fig. 1 have been represented by the relationships among elements in the MCE-based joint spectrum matrix $H(f)$, which is defined in Fig. 2 and also encompasses the physical entities such as RES $\tilde{S}^{bb}(f)$, the stationary-state wind spectrum $S(f)$, the wave spectrum $S^w(f)$ and the CPSD. It is also worth noting that there are six zones in Fig. 2, where the zones along the diagonal direction represent the spectral components in their own domains whilst the non-diagonal zones reflect the coupled spectral components across the domains.

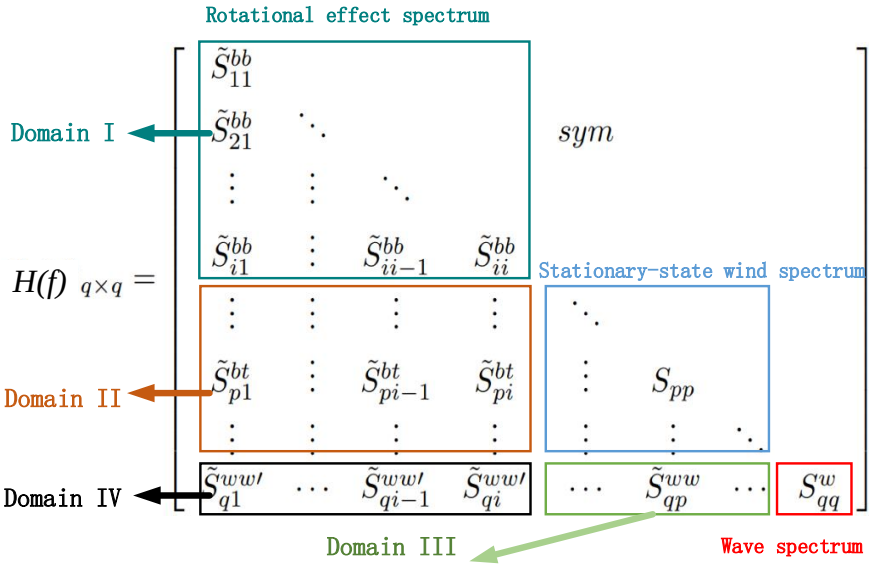

Fig. 2: MCE-based multifield spectrum matrix.

In general, the stationary-state winds represented in the joint spectrum matrix are decomposed by Cholesky method in the process of wind load reconstructions. As the significant energy differences between wind and wave in the near-zero frequency region, the non-convergent results can not be guaranteed when the MCE-based joint power spectrum matrix is decomposed into the Non-Hermite positive definite matrix using Cholesky method. To improve the convergence and robustness of the matrix decomposition, the improved square root method has been applied for the decomposition of the MCE-based joint spectrum matrix formulated in Eq. (34):

$$H(f)_{q\times q} = L(f)_{q\times q} D_{q\times q} L(f)_{q\times q}{}^{*} \tag{34}$$

where $L_{q\times q}$ and $D_{q\times q}$ represent the lower triangular and diagonal matrices obtained by the improved square root method, respectively.

Subsequently, the amplitudes and phase angles in Eq. (2) can be determined by Eq. (35) using the decomposed components.

$$\begin{cases} A(\omega)_{q\times q} = \sqrt{2\Delta w}\left|L(w)_{q\times q}\sqrt{D_{q\times q}}\right| \\ \beta(\omega)_{q\times q} = \tan^{-1}\left(\dfrac{\mathrm{lm}[L(w)_{q\times q}\sqrt{D_{q\times q}}]}{\mathrm{Re}[L(w)_{q\times q}\sqrt{D_{q\times q}}]}\right) \end{cases} ,0 \le w \le w_N \tag{35}$$

where Δw is the frequency resolution and w_N is the upper cut-off frequency of the wind load.

Once the time series of wind speeds are reconstructed using Eq. (2), the loads in the different domains of the offshore wind turbine could be accurately evaluated by Eq. (36) under the considerations of MCE. For example, the normal aerodynamic loads on the blades can be determined using BEM, and loads on the tower from the wind and

waves can be obtained by the multifield interactions of offshore wind turbines established by the MCE-based joint power spectrum matrix.

$$F_{load} = \begin{cases} \frac{1}{2}\rho c[(\bar{U}+u_b)(1-a')]^2 + [\Omega r\,(1+a'')]^2\, C_N & ,B_{wind} \\ \frac{1}{2}\rho C_d u_t^2 A_w & ,T_{wind} \\ \frac{\pi D_t^2}{4} C_M \rho_w \dot{u_f} z_t + \frac{\rho_w}{2} C_D D_t u_f |u_f| z_t & ,T_{wave} \end{cases} \tag{36}$$

where B_{wind}, T_{wind} and T_{wave} denote the wind action on the blades, the wind action on the tower and the wave action on the tower, respectively; a' and a'' are induction factors of the axial and tangential velocities, respectively; Ω denotes the rotating speed of the blade; C_N is the normal coefficient of the blade elementu_b denotes the wind speed on the blade; A_w represents the effective windward area; u_t is the wind speed on the tower; C_M and C_D mean the mass and drag coefficients of the wave, respectively; ρ_w is the water density; D_t means the diameter of the tower; z_t represents the tower strip length; $\dot{u_f}$ and u_f are the acceleration and velocity of the fluid particle, respectively.

A flowchart illustrating the theoretical process is given in Fig. 3.

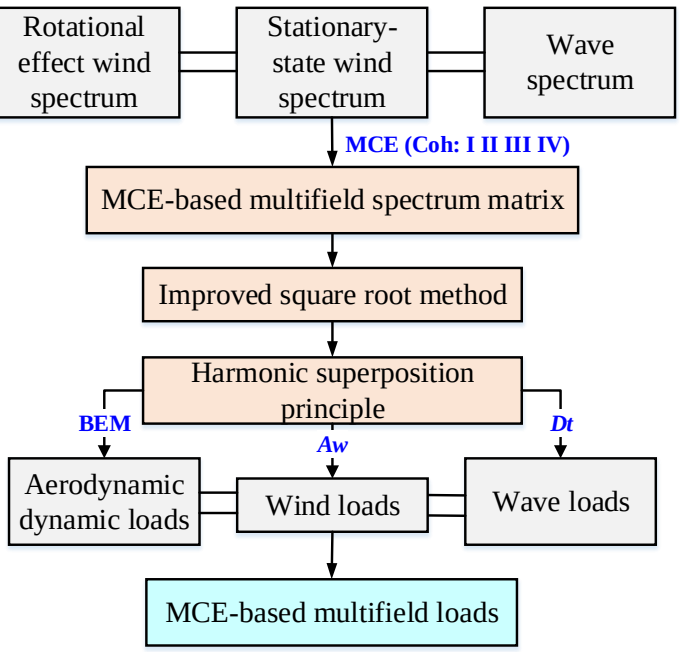

Fig. 3: Flowchart of MCE-based multifield loads theory.

4. Numerical validation and analysis

In this section, numerical analysis of the wind speed distribution over the rotational domain of offshore wind turbines has been conducted to demonstrate the accuracy and effectiveness of RES (Rotational effect spectrum) in the proposed method. Furthermore, MCE (multivariate coherence effect)-based wind loads have been accurately calculated using the multifield spectral decomposition. Finally, structural responses of offshore wind turbines have been

analyzed to illustrate the importance of the combination of RES with MCE for the accurate estimation of multifield loads.

4.1. Validation of the RES

The benchmark model used to evaluate the correctness of the proposed MCE-based RES method for dynamic analysis is originated from National Renewable Energy Laboratory (NREL) 5MW-OC3 Hywind floating offshore wind turbine (Jonkman, 2010), whose structural characteristics and specified environmental parameters are provided in Table 1.

Table 1: Properties and environmental parameters of the floating offshore wind turbine

Property Characteristics	Parameter Name	Parameter values
Physical properties	Max. rated power	5 MW
	Number of blades	3
	Rotor diameter	126m
	Rotor speed	6.9 $\sim$ 12.1rpm
	1p, 2p, 3p at rated power	0.201 Hz, 0.403 Hz, 0.605 Hz
Atmospheric properties	Surface roughness	0.005m
	Wind speed at hub	3$\sim$25m/s
	Coherence decay factor	8.8
Wave properties	Significant wave height	1.6 $\sim$ 5.9m
	Peak spectral period range	4.2 $\sim$ 5.6s
	Scale parameter	0.00384096
	Shape parameters(k,y)	5.5, 45.132

To evaluate the influence of RES derived in Eq. (21) on the performance of wind turbines, RES has been initially constructed using the Karman spectrum that is formulated by Eq. (37) as the source spectrum for the numerical studies (He et al., 2013). The comparison results between RES and the Karman spectrum in the frequency domain considering the mean wind speed of 25m/s at the height of 90m from the reference position of the sea level have been shown in Fig. 4(a), where the energy transfer from low to high frequencies can be clearly observed under the consideration of RES. It has been also noted that the dominant frequency of the stationary-state wind has been identified as 0.012 Hz, which exactly corresponds to the maximum energy of the Karman spectrum. With the proposed method, the model established has the ability to retain the peak frequencies as estimated by the Karman spectrum and predict the decreased amplitudes of energy peaks corresponding to 0.201 Hz, 0.403 Hz and 0.605 Hz (1P, 2P, 3P), indicating that the lower rotational frequency represents the more energetic contribution.

$$\frac{f \cdot S_{karman}(f)}{\sigma_u^2} = \frac{4fL_c/\bar{U}}{\left[1 + 70.8\left(fL_c/\bar{U}\right)^2\right]^{5/6}} \tag{37}$$

where $S_{karman}(f)$ is the Karman spectrum and σ_u is the standard deviation.

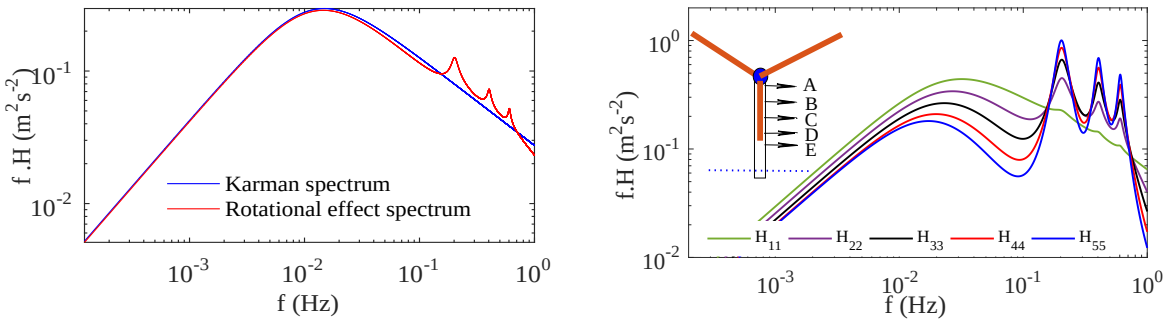

Fig. 4: The analysis of RES: (a) The comparison of Karman and RES, (b) The RES profiles at different heights in the range of 12m to 85m.

To capture the features of RES in the frequency domain at different radiuses of the blade, the APSD ($H_{11} \sim H_{55}$) have been calculated at the positions A $\sim$ E accordingly, where the radiuses measured from the hub with the values of 2.6m, 22.6m, 42.6m, 62.6m and 75.6m, or 85m, 65m, 45m, 25m and 12m from the sea level shown in Fig. 4(b). It can be observed in Fig. 4(b) that H_{11} (at Point A) has converted into the Karman-like wind spectrum in the vicinity of the center of the hub (at the distance of only 2.6m), and the rotational effect has become more pronounced as the distance from the hub center has been increased. For example, the energy amplitude corresponding to 0.201 Hz at the radius of 45m has been increased by 47.54% as compared with the value at 25m. In summary, results have demonstrated that the model by the developed method considering RES has the ability to reflect multiple rotational frequencies, which are vital to the resonance analysis of offshore wind turbine components.

4.2. Quantitative analysis of MCE-based CPSD

As discussed in Section 3.2, mathematical formulations of the MCE-based CPSD defined by Eqs. (10), (15), (18) and (19) have explicitly described the interactions with the coherence function and the APSD of the wind or waves. It is vital to explore impacts of the multivariate coherence functions on the CPSD over the four domains in Fig. 1. First, points in Fig. 5 at a height of 6m (Point F) and 0m (Point G) measured from the sea level have been used to generate the stationary-state wind spectrum (H_{66}) and JONSWAP spectrum (H_{77}), respectively. It has been noted that the CPSDs of wind speeds at different positions shown in Fig. 5(a) have successfully captured the multiple rotational frequencies and the rotational effect has becomes more pronounced with the closer distance between two points. However, the remarkable attenuation of peaks at the multiple rotational frequencies has been observed in Fig. 5(b). The higher the rotational frequency is, the more the energy attenuates. For example, the values of H_{46} have been reduced by 63.5% and 86.17% than the results of H_{56} at the first and second frequencies, respectively. Meanwhile, the distance-dependent behaviour of wind-wave coherence has been observed in Figs. 5(c) and (d), indicating that the coherent distance is a dominant factor to reflect the energy of the CPSD. It is also worth noting that the energy represented by CPSD between the rotational wind field and the wave is much higher than that of the CPSD between the stationary-state wind field and the wave, as shown in Figs. 5(c) and (d). This can be explained by the fact that the peaks at multiple rotational frequencies have stood for the higher energy contributions as compared to the results by

the Karman spectrum when the same height has been assumed. Considering the higher energy weight, it is necessary to pay more attention on CPSD in Domain IV than Domain III for accurate analysis of loads applied on floating wind turbine structures with blades close to the sea level.

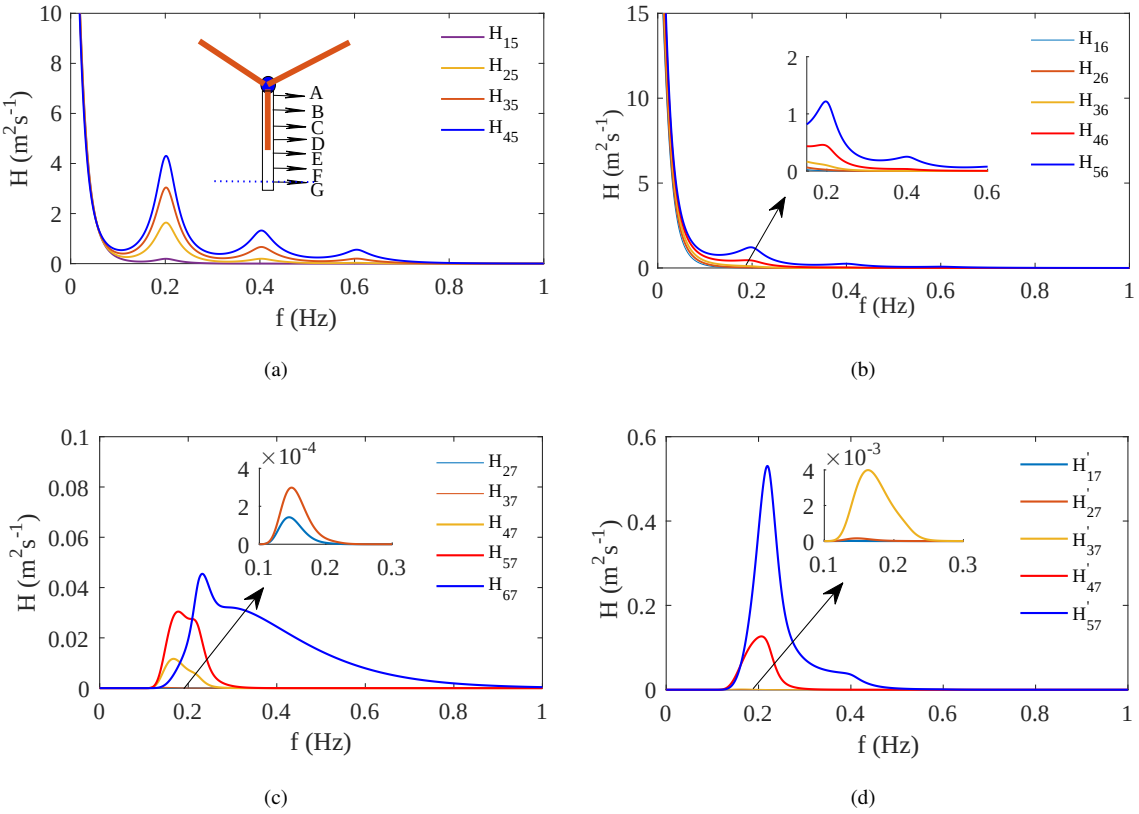

Fig. 5: Characteristics of MCE-based CPSD (H_{ij} i, j=1, $\cdots$, 7 and the subscripts 1∼7 correspond to Points A∼G): (a) Domain I, (b) Domain II, (c) Domain III, (d) Domain IV.

4.3. MCE-based multifield spectrum verification

As the energy components of the formulated multifield spectrum depend on the joint power spectrum matrix, it is vital to establish the MCE-based multifield spectrum for construct the accurate joint power spectrum matrix under the consideration of coupling effects. Based on the equations for the MCE-based CPSD defined in Section 3.3, time series of the wind speed and wave heights for offshore wind turbines have been reconstructed using the harmonic superposition principle. Furthermore, the accuracy of the proposed method will be verified by the comparison of the theoretical spectrum with the simulated spectrum obtained by Fourier transform of time series at the position with the distance of 12m from the sea level. The pre-specified frequency range is adopted between 0 and 1 Hz with the increment of 0.0001 to accurately cover the frequency range of wind speeds and random waves. The reconstructed results of wind speeds and wave heights in the time and frequency domains have been shown in Fig. 6. It has been observed that RES, Karman spectrum and JONSAWP wave spectrum have a good agreement with the corresponding theoretical spectrum in the frequency domain, indicating the accuracy of the reconstructed time series. Moreover, the

advance of the MCE-based method for simulations of offshore wind field lies in the fact that the time or frequency ranges of the stationary-state wind speed, rotational wind speed and wave height are exactly same due to the simultaneous decomposition of the coherent power spectrum matrix for the load reconstruction. This has been proved by the results shown in Fig. 6. From the practical point of views, the accurate assessment of structural dynamic responses of offshore wind turbines relies not only on external environmental factors such as wind speeds and wave heights, also on the combination of shape parameters such as the airfoil shape and tower surface area for the reliable prediction of complex environmental loads. Therefore, results in this section have verified the correctness of the multifield spectral analysis, which will provide a solid foundation for subsequent load calculations and accurate dynamic responses of offshore wind turbines.

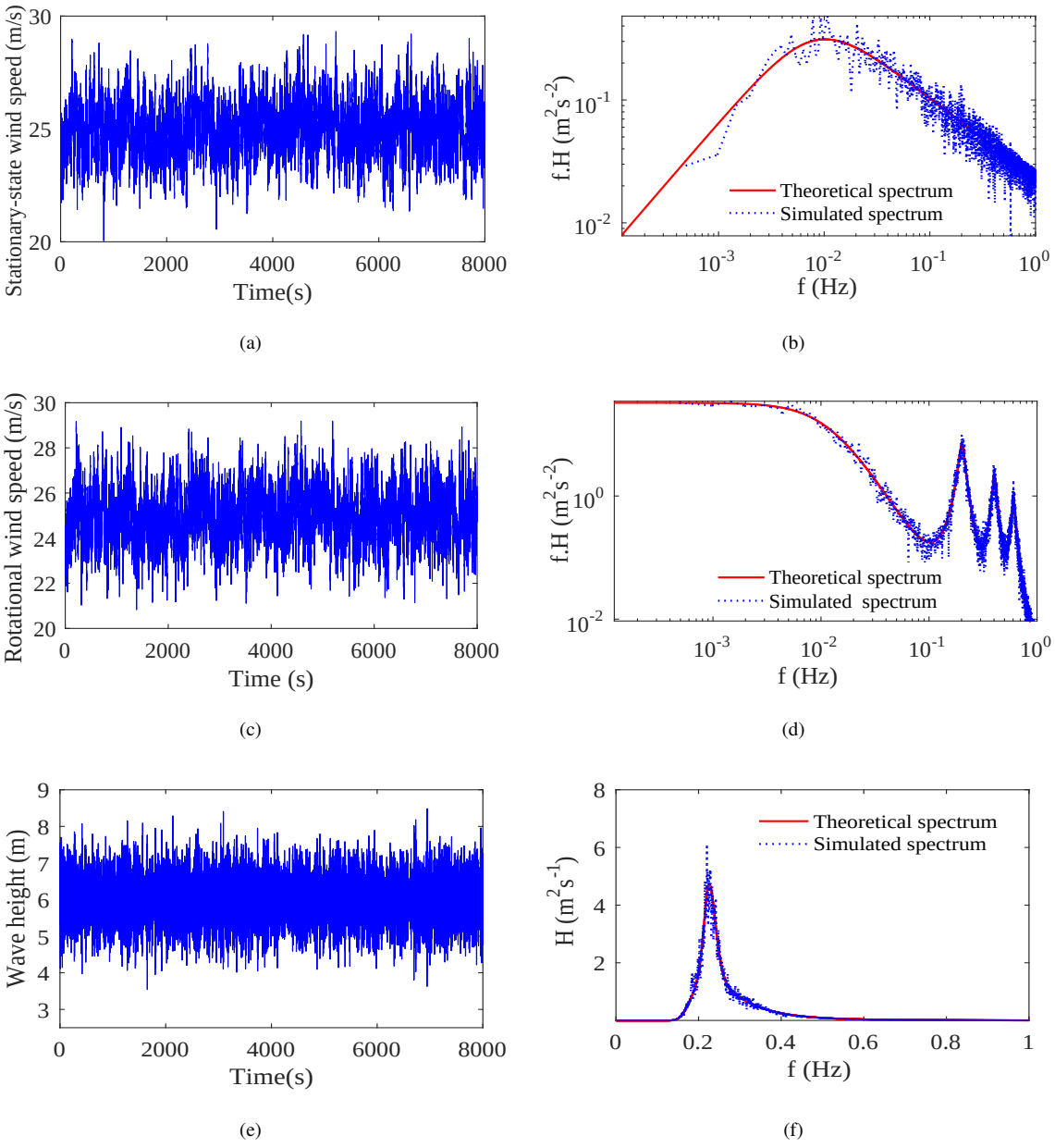

Fig. 6: The reconstructed wind speed and wave height by the proposed method: (a) Stationary-state wind speed in time domain, (b) Stationary-state wind speed in frequency domain, (c) Rotational wind speed in time domain, (d) Rotational wind speed in frequency domain, (e) Wave height in time domain, (d) Wave height in frequency domain.

4.4. Evaluation of the MCE mechanism

To further investigate the effect of multivariate coherences on the wind speed and wave height, the reconstructed results in the time and frequency domains with and without the consideration of MCE (Ti and Zhou, 2022) have been compared and the corresponding multifield loads applied on the structure have been evaluated. In Fig. 7, results by both coherent and non-coherent spectral analysis have been compared for the rotational wind speed, stationary-state

wind speed and wave height sequences at the positions of 12m, 6m and 0m above the sea level, respectively. It has been observed that the reconstructed time series of wind speeds and wave heights by the proposed method have demonstrated remarkable differences from the results obtained by the non-coherent spectral analysis, and the MSE (Mean Square Errors) valued has been also provided to validate the accuracy of computations. Meanwhile, the coherence effects have a significant impact on the frequency amplitude of the reconstructed results and the sparser distributions in the range of low frequencies can be observed as compared with the simulations by the non-coherent analysis. Based on these observations, Fig. 8 has illustrated the variation of frequency amplitudes in the RES, stationary-state wind spectrum and wave spectrum under the consideration of MCE. The simulation results have demonstrated that the energy concentrations have occurred at 0.2, 0.4 and 0.6 Hz in the RES, at 0.01 Hz in the stationary-state wind spectrum and at 0.2 Hz in the wave spectrum, indicating the good agreement with the characteristic frequencies of multifield spectrum shown in Fig. 6.

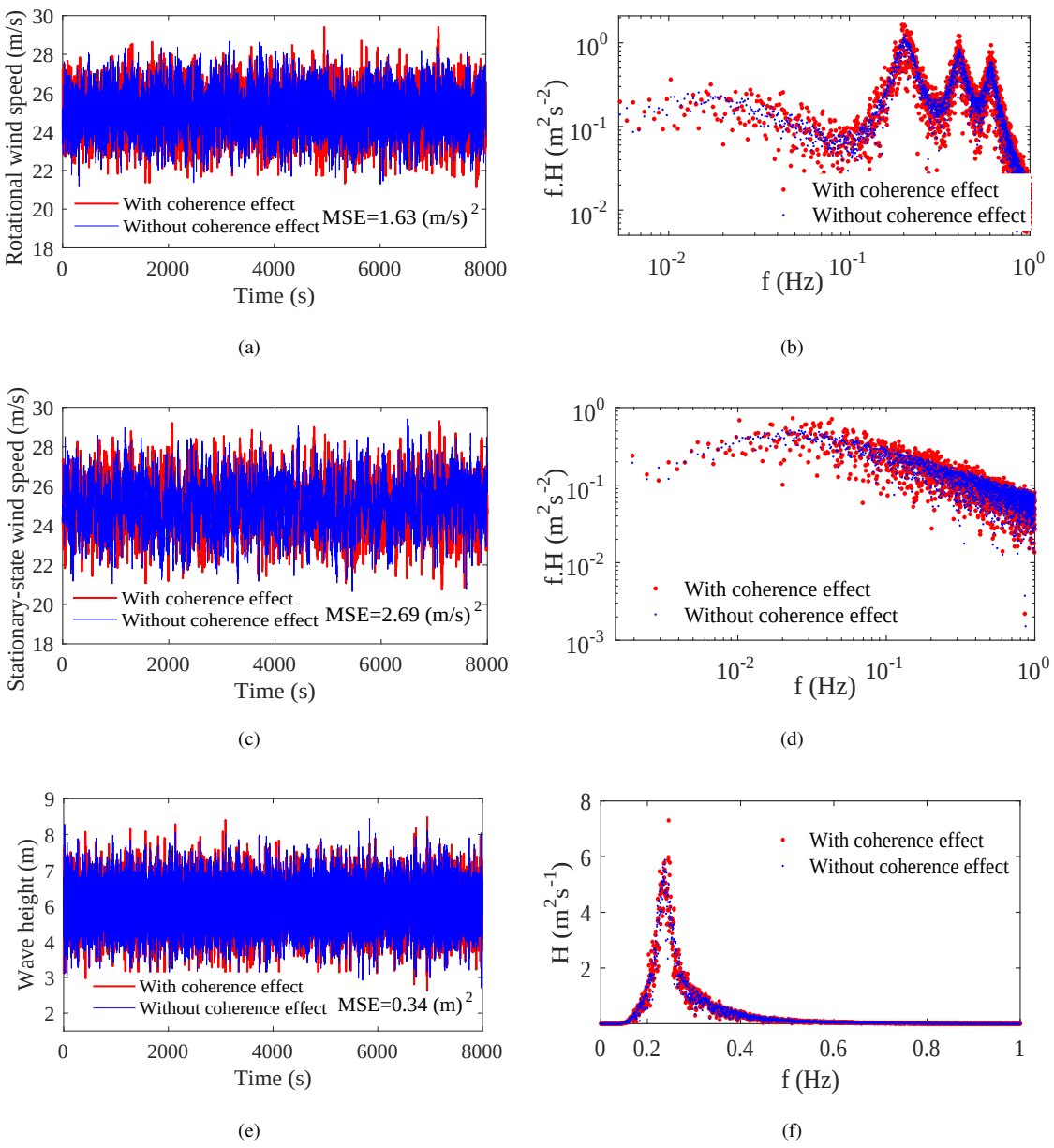

Fig. 7: Comparison results of the wind speed and wave height with and without coherence effects: (a) Stationary-state wind speed in time domain, (b) Stationary-state wind speed in frequency domain, (c) Rotational wind speed in time domain, (d) Rotational wind speed in frequency domain, (e) Wave height in time domain, (d) Wave height in frequency domain.

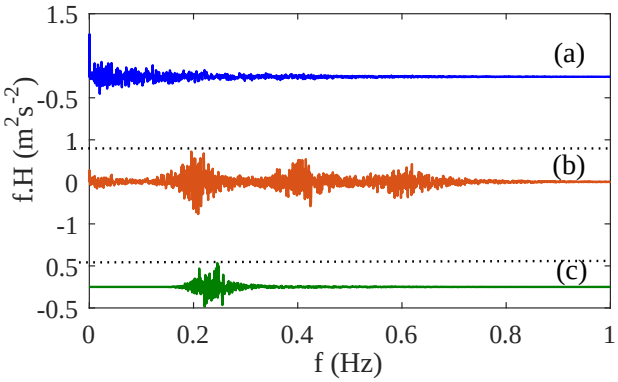

Fig. 8: The difference of energy between the coherent and non-coherent analysis using: (a) Stationary-state wind spectrum, (b)Rotational effect wind spectrum (c) Wave spectrum.

Furthermore, MCE-based multifield loads within 450s have been shown in Fig. 9, where the coupled loads considering the coherence across different domains can represent the features with more details than the results by the non-coherent analysis. It is worth noting that the stationary-state wind loads in Fig. 9(b) have shown the unidirectional fluctuation due to the tower shadow effect, leading to the difference from the oscillatory fluctuation of the stationary-state wind speed in Fig. 7(c). However, as the cyclic trajectory of the water quality points around the tower has occurred, wave forces show a tendency of oscillations in Fig. 9(c) . In conclusion, numerical results have showed that the MCE-based method has the ability to accurately model amplitudes of the wind speed, wave heights and multifield loads.

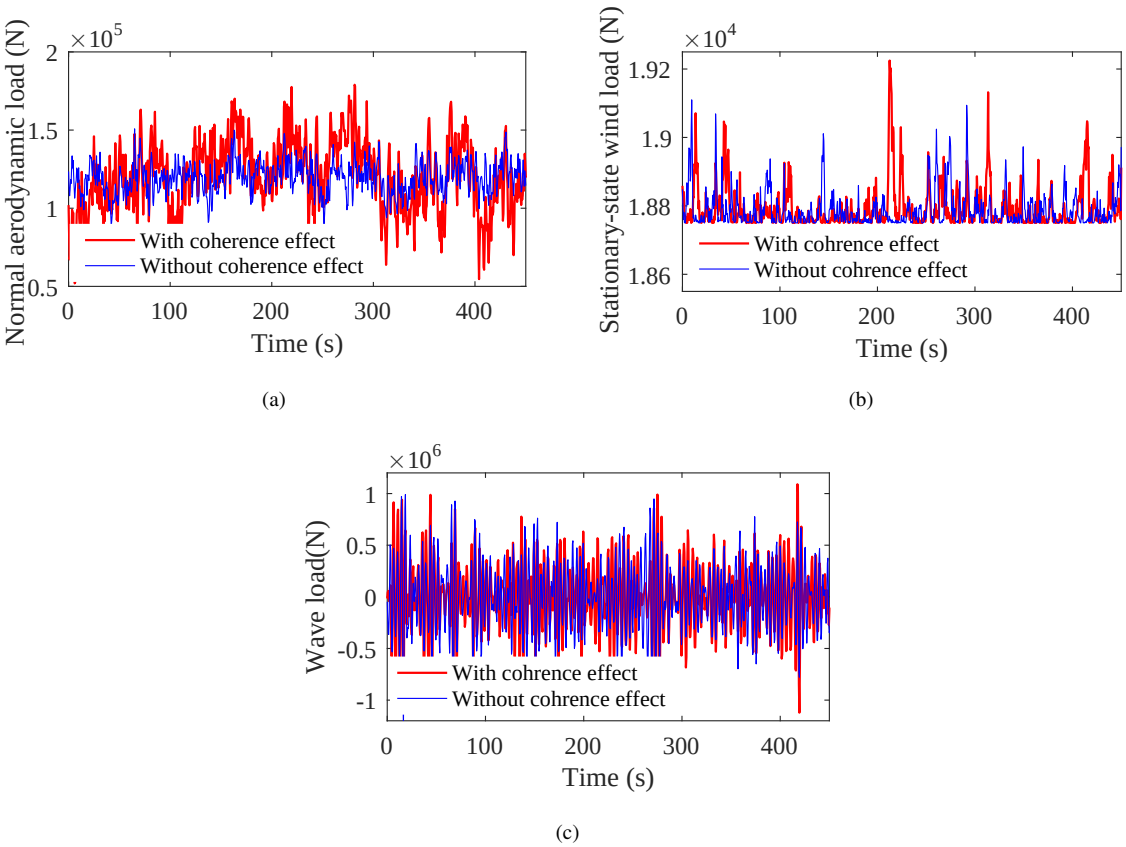

Fig. 9: Comparison results of multifield loads with and without coherence effects: (a) Aerodynamic load on the blade, (b) Wind load on the tower, (c) Wave load on the tower.

4.5. Comparison with SNL method

In this section, the advantages of the proposed method have been demonstrated by the result comparison with the typical time-domain SNL method (Moriarty and Hansen, 2005), in which the rotating wind speed by sequentially sampling the wind profile in front of the rotor was obtained. Both the height and width of the wind field considered in the research were defined as 145m. During the rotational sampling, 961 wind speed points were uniformly arranged to cover the entire offshore wind turbine. The reference mean wind speed at the hub was 11.4m/s and the rotational sampling points were set at 25m from the hub. Stationary-state wind and wave spectrum have been constructed at Points F and G, respectively, as shown in Fig. 5(a). The wind speed series by SNL and MCE-based RES have been converted to the values in the frequency domain and have indicated that two methods have the ability to accurately obtain multiple rotational frequencies of the blade with slight differences shown in Fig. 10.

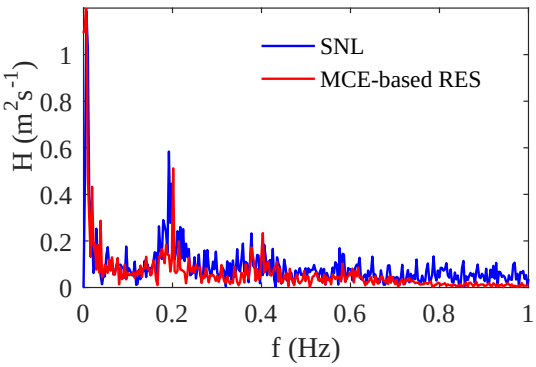

Fig. 10: Comparison results of wind speed series between SNL and MCE-based RES in frequency domain.

The APSD source spectrums in SNL and MCE-based RES methods shown in Fig. 11(a) have described the stationary-state wind spectrum without the capability of representing the physical mechanism of rotational spectrum. As compared with the SNL method, the coupling energy components across Domains III and IV have been identified in the calculation of CPSD by the proposed MCE-based method shown in Fig. 11(b), indicating the importance of the coherent effect between the constructed wind and waves. In summary, the above results have demonstrated that the proposed MCE-based RES method has enables the accurate characterization of the rotational spectrum and the comprehensive embodiment of the wind wave coupling.

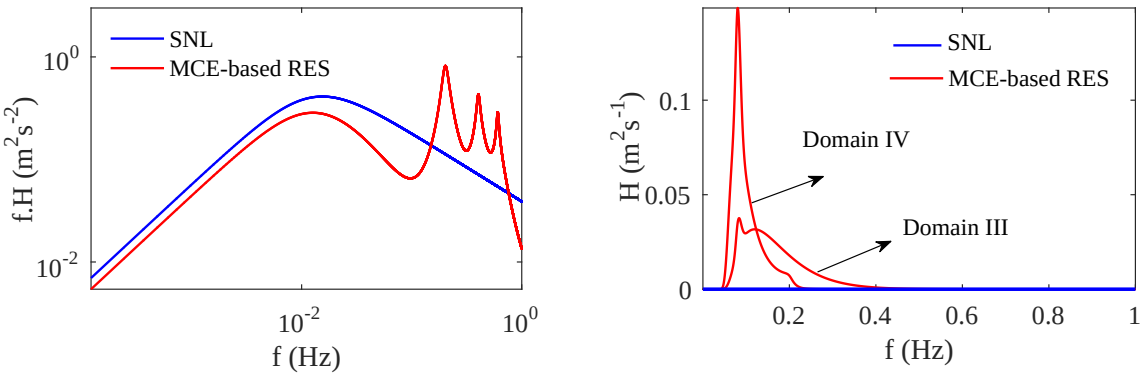

(a) (b)

Fig. 11: Comparison results of PSD between SNL and MCE-based RES: (a) The APSD source spectrum, (b) The CPSD for the coupling of wind and waves.

4.6. Dynamics analysis of blades subject to MCE-based loads

The aerodynamic load is one of the most critical factors dominating blade vibrations of offshore wind turbines. As a representative example, a simplified blade model by Matlab has been developed to evaluate the synthetic effects of rotational and coherence effects on the flapwise vibration. The flapwise vibration has been formulated by a function

of the generalized coordinates ($q1$ and $q2$) and mode shapes ($\emptyset_1$ and $\emptyset_2$) as shown in Fig. 12, and the kinetic equations can be derived using the Lagrangian method as follows:

$$m_0\ddot{q}(t) + c_0\dot{q}(t) + k_0 q(t) = F_{flap}(\dot{q}, t) + f_g(t) \tag{38}$$

where m_0 and c_0 are the modal mass and damping matrices, respectively; k_0 denotes the modal stiffness matrix, which reflects both the blade geometric stiffness and the stiffness associated with the harden effect due to rotation. $F_{flap}(\dot{q}, t)$ means the generalized aerodynamic load by the proposed MCE-based method; $f_g(t)$ represents the gravity load.

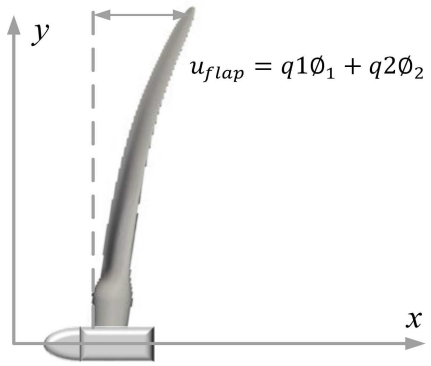

Fig. 12: A simplified blade model.

The correctness and efficiency of the simplified blade model has been verified by OpenFAST (Matha, 2010) in terms of natural frequencies, which are 0.74 Hz and 2.07 Hz for the first and second natural frequencies calculated by OpenFAST and 0.74 Hz and 2.08 Hz by the simplified blade model. Furthermore, the comparison results in the time domain at 11.4m/s mean wind speed have been shown in Fig. 13 to demonstrate the good agreement of responses by the developed model and OpenFAST.

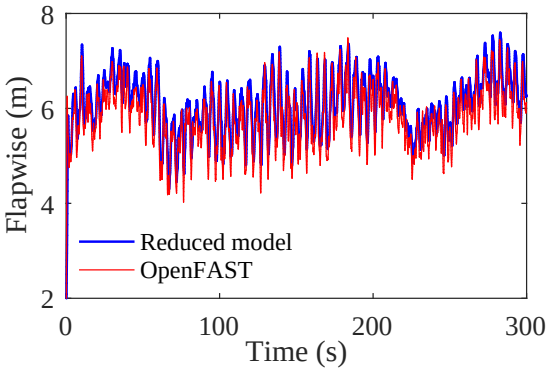

Fig. 13: The flapwise displacement comparison of a simplified blade model.

To investigate the dynamic performances of blades subject to both RES and MCE-based loads, the blade flapwise displacement has been calculated considering the mean wind speed of 11.4m/s. It has been observed in Fig. 14 that the displacement by the analysis considering RES (the rotational effect) to reflect the actual blade load under operation is remarkably smaller than the result obtained by the simulation without the consideration of RES. This phenomenon can be interpreted by the higher blade stiffness resulting from the stiffening effect of the actual blade rotation. Moreover, the response by the RES-based analysis has accurately reflected the characteristics (multiple rotational frequencies of the blade) in the frequency domain, whereas the result by the analysis without RES has the limited capability to demonstrate this feature as only the first order natural frequency of the blade can be obtained under the stationary-state condition.

In Fig. 15, the effect of MCE-based loads on the blade dynamic displacement has been illustrated under the marine environmental condition. It is worthy of note that the blade displacement by the proposed MCE-based method has been predicted with the larger magnitudes in the time domain and the higher energy at the multiple rotational frequencies in the frequency domain, as compared with the response based non-coherent analysis(Das et al., 2019).

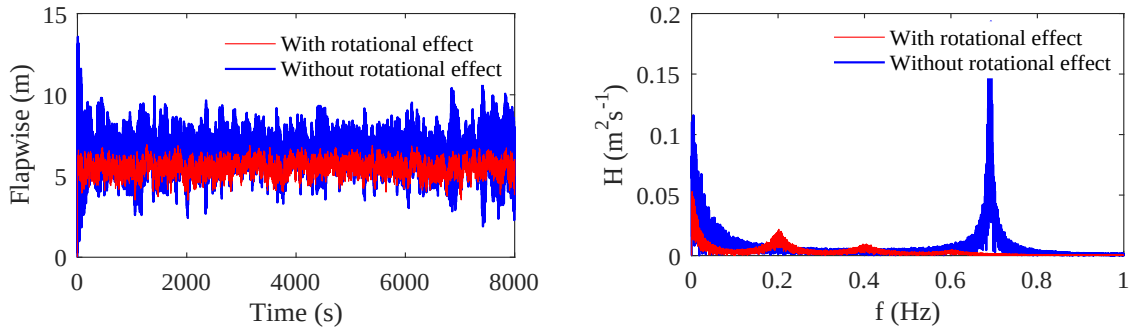

(a) (b)

Fig. 14: Comparison results of flapwise displacements with and without rotational effects: (a) Flapwise displacements in time domain, (b) Flapwise displacements in frequency domain.

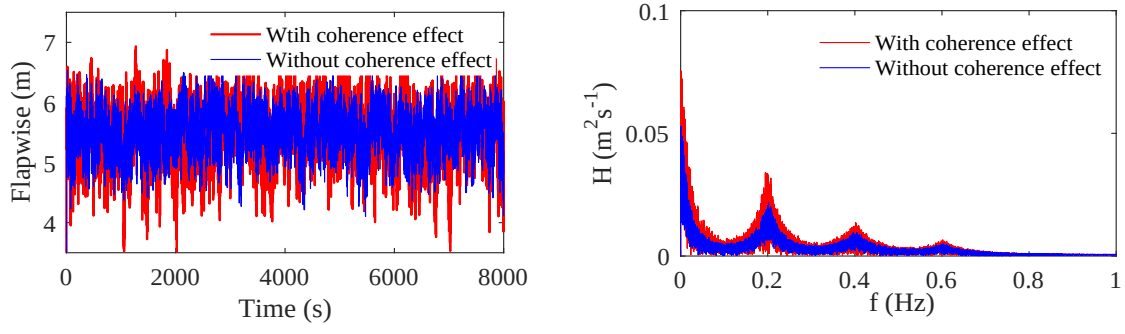

(a) (b)

Fig. 15: Comparison results of flapwise displacements with and without coherence effects: (a) Flapwise displacements in time domain, (b) Flapwise displacements in frequency domain.

To accurately assess both the rotational and coherence effects on the blade flapwise displacement under the complex working conditions, parameters including the maximum wave height and peak spectral period range shown in Fig. 16 to reflect the wind-wave interaction under different wind speeds should be determined (Jonkman, 2007). In this study, the flapwise vibration induced by the mean wind speeds of 3 $\sim$25m/s at the hub of the offshore turbine has been shown in Fig. 17, where the sum of the third quartile (Q3) and the interquartile range (IQR) have been applied to statistically evaluate the maximum and the mean values of responses.

As shown in Fig. 17, the maximum and mean values of the blade flapwise deflection have increased and then decreased with the increase of wind speed due to the pitch control. It has been noted that the maximum value of the blade response by the analysis considering both rotational and coherence effects has been reduced by 40.97% at 11.4m/s mean wind speed, as compared with the simulation by the analysis under the consideration of the coherence effect only. Moreover, the predicted maximum value has been averagely larger by 6.07% than the result by the analysis coupled with the rotational effect only. Meanwhile, more detailed comparison results of flapwise displacements with and without rotational and coherent effects have been explicitly quantified in Table 2. Results have shown that the rotational effect-based method has underestimated the flapwise deflection, especially for both the power generation at low wind speeds (for example, 3m/s) and the pitch control at high wind speeds (e.g., 23m/s), leading to the serious safety risk and critical economic loss. It has been worth noting that the flapwise response has been overestimated when only coherent effects have been considered, while this response has been underestimated with the consideration of the rotational effect only. Furthermore, the larger increase extent of the flapwise response has been observed as compared with the decrease extend. Therefore, it is vital to accurately assess multifield loads for the analysis of more reliable structural dynamics of offshore wind turbines. Based on these observations, the proposed approach has demonstrated the ability to estimate multifield loads under the consideration of the rotational and coherence effects, and provide engineers a useful design strategy with the capability of bounded analyses in the complex marine environment. Furthermore, the similar conclusion can be drawn in terms of the mean values, indicating that an inappropriate overall shift in the calculation of the blade response can be caused by the analysis considering the coherence effect only. In conclusion, it has been proved that the proposed MCE-based method has the ability to accurately predict the multiple rotational frequencies of the rotational blade and establish a multi-domain correlation under the marine environment, owing to its capability of reliable estimation of multifiled loads for the dynamic responses of wind turbine structures.

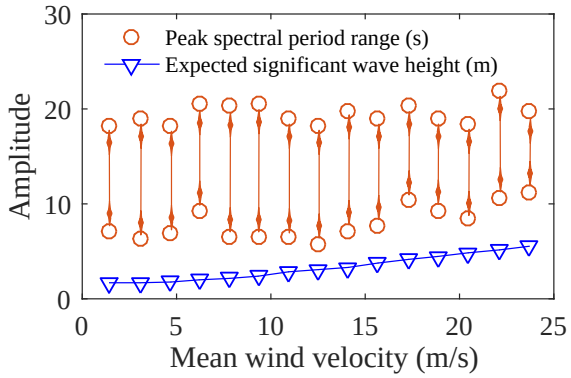

Fig. 16: Wind and wave correlation of sea conditions

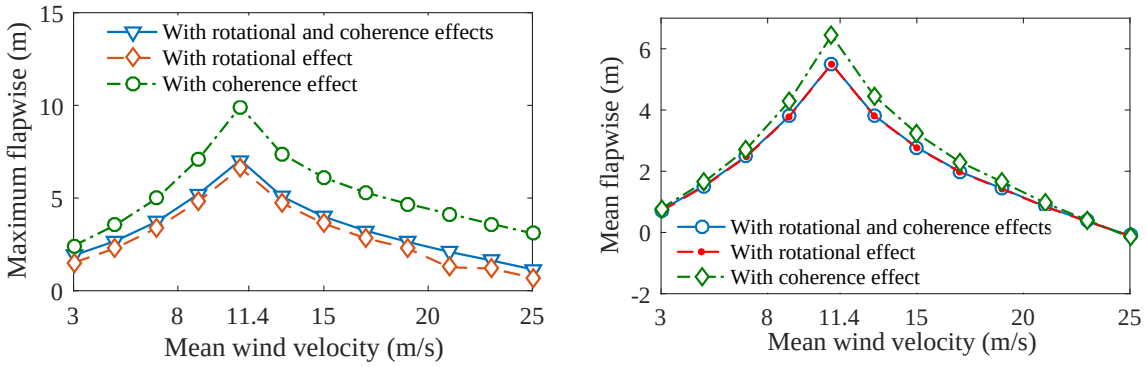

(a) (b)

Fig. 17: Comparison results of flapwise displacements with and without rotational and coherence effects: (a) Maximum flapwise values, (b) Mean flapwise values.

Table 2: Quantitative comparison of flapwise displacements with and without rotational and coherence effects.

Mean wind velocity (m/s)	With rotational and coherence effects		With rotational effect		With coherence effect	
	Maximum flapwise (m)	Mean flapwise (m)	Maximum flapwise decrease percentage (%)	Mean flapwise decrease percentage (%)	Maximum flapwise increase percentage (%)	Mean flapwise increase percentage (%)
3	1.906	0.725	20.676	4.435	27.061	7.693
7	3.730	2.493	9.054	0.744	33.803	9.307
11	7.047	5.509	6.068	0.237	40.975	16.818
15	3.993	2.779	9.333	0.491	52.814	16.354
19	2.640	1.435	13.157	0.804	77.765	15.183
23	1.641	0.369	27.102	3.217	120.034	8.367

5. Summary and conclusions

In this paper, a novel multivariate coherence effect (MCE)-based rotational effect spectrum (RES) method has been proposed to achieve the accurate construction of loads on offshore wind turbines with the consideration of rotational wind effect and waves. Two novelties and one contribution of this study are mainly listed as follows: (i) Multiple rotational frequencies of the blade are accurately obtained through the novel MCE-based RES method. (ii) The loads induced by couplings of multivariately correlated domains are determined using the joint MCE-based spectrum matrix. (iii) The quantitative assessment of the influence of rotational and coherent effects on the blade flapwise is performed to highlight the importance of this research. Firstly, to establish correlations of offshore multifield loads, the MCE-based joint power spectrum matrix is derived based on the theoretical analysis of RES and MCE. Secondly, the MCE-based multifield spectrum is quantitatively evaluated throughout an example of 5MW offshore wind turbines. Thirdly, aerodynamic loads, wind loads and wave loads are accurately calculated using the multifield spectrum matrix. Finally, the rotational and coherent effects on dynamic responses of the blade flapwise vibration is comprehensively assessed to emphasize the importance of the proposed MCE-based method.

The main findings in this research are summarized as follows:

(1) The RES enables the accurate estimation of multiple rotational frequencies of 0.201 Hz, 0.403 Hz and 0.605 Hz (1P, 2P, 3P) for blades in a 5MW offshore wind turbine.

(2) The influences of the rotational wind and waves on the load redistribution are more pronounced in rotational and wave coherence domain (Domain IV) than stationary-state and wave domain (Domain III) at the same height due to the stronger coherence.

(3) The reconstructed MCE-based multifield spectrum has the good agreement with the theoretical spectrum. Moreover, the time or frequency ranges of the reconstructed stationary-state wind speed, rotational wind speed and wave height are identical, respectively.

(4) The maximal flapwise deflection by the MCE-based RES method is smaller as compared with the result by the pure coherence effect-based analysis, while the slightly larger deflection is observed than the prediction by the analysis considering the rotational effect only.

The new mechanisms and laws by considering MCE have been concluded as follows:

(1) The degree of MCE is related to both the coherence distance and source spectral energy: The closer the distance and the higher the spectral energy lead to the higher the coherence.

(2) The coupling and synchronization of the wind and waves originate from the constructed MCE-based CPSD and the identical coherent power spectral matrix, respectively.

(3) The coherence effects cause complex spectral energy components and also reduce the flapwise response.

The proposed MCE-based RES method in this study is scoped for the accurate evaluation of multifield loads induced by the effects of rotating blades on wind velocity and the interactions among multiple components such as wind, waves and the structure. This will lead to the cost-effective design of offshore wind turbines, particularly floating turbines in deep sea. The limitations of this research include: (i) The developed model in this paper has not been validated by the field offshore experimental tests. (ii) As a specific example is studied in Section 4.6, the findings are completely limited to this research. In future studies, the number and diversity of the field data will be considered to construct a MCE-based RES model with the broad applicability and feasibility.

6. Acknowledgements

The authors acknowledge the financial support of the National Outstanding Youth Science Fund Project of National Natural Science Foundation of China (52125106) and the National Natural Science Foundation project (U22A20243).

References

Amini, A., Abdollahi, A., Hariri-Ardebili, M., Lall, U., 2021. Copula-based reliability and sensitivity analysis of aging dams: Adaptive kriging and polynomial chaos kriging methods. Applied Soft Computing 109, 107524. doi:10.1016/j.asoc.2021.107524.

Andersen, O.J., Løvseth, J., 2006. The frøya database and maritime boundary layer wind description. Marine Structures 19, 173–192. doi:10.1016/j.marstruc.2006.07.003.

Banerjee, A., Chakraborty, T., Matsagar, V., Achmus, M., 2019. Dynamic analysis of an offshore wind turbine under random wind and wave excitation with soil-structure interaction and blade tower coupling. Soil Dynamics and Earthquake Engineering 125, 105699. doi:10.1016/j.soildyn.2019.05.038.

Bi, K., Hao, H., 2012. Modelling and simulation of spatially varying earthquake ground motions at sites with varying conditions. Probabilistic Engineering Mechanics 29, 92–104. doi:10.1016/j.probengmech.2011.09.002.

Burlibaşa, A., Ceangă, E., 2013. Rotationally sampled spectrum approach for simulation of wind speed turbulence in large wind turbines. Applied Energy 111, 624–635. doi:10.1016/j.apenergy.2013.05.002.

Chen, J., Song, Y., Peng, Y., Nielsen, S.R., Zhang, Z., 2020. An efficient rotational sampling method of wind fields for wind turbine blade fatigue analysis. Renewable Energy 146, 2170–2187. doi:10.1016/j.renene.2019.08.015.

Chen, J., Yang, R., Ma, R., 2015. Wind field simulation of large horizontal-axis wind turbine system under different operating conditions. The Structural Design of Tall and Special Buildings 24, 973–988. doi:10.1002/tal.1221.

Cheng, Z., Wang, K., Gao, Z., Moan, T., 2016. A comparative study on dynamic responses of spar-type floating horizontal and vertical axis wind turbines. Wind Energy 20, 305–323. doi:10.1002/we.2007.

Colwell, S., Basu, B., 2009. Tuned liquid column dampers in offshore wind turbines for structural control. Engineering Structures 31, 358–368. doi:10.1016/j.engstruct.2008.09.001.

Connell, J., 1982. The spectrum of wind speed fluctuations encountered by a rotating blade of a wind energy conversion system. Solar Energy 29, 363–375. doi:10.1016/0038-092x(82)90072-x.

Damgaard, M., Ibsen, L., Andersen, L., Andersen, J., 2013. Cross-wind modal properties of offshore wind turbines identified by full scale testing. Journal of Wind Engineering and Industrial Aerodynamics 116, 94–108. doi:10.1016/j.jweia.2013.03.003.

Das, S., Sajeer, M.M., Chakraborty, A., 2019. Vibration control of horizontal axis offshore wind turbine blade using SMA stiffener. Smart Materials and Structures 28, 095025. doi:10.1088/1361-665x/ab1174.

Datta, T., Jain, A., 1990. Response of articulated tower platforms to random wind and wave forces. Computers & Structures 34, 137–144. doi:10.1016/0045-7949(90)90307-n.

Davenport, A.G., 1962. The spectrum of horizontal gustiness near the ground in high winds. Quarterly Journal of the Royal Meteorological Society 88, 197–198. doi:10.1002/qj.49708837618.

Davenport, A.G., 1963. The relationship of wind structure to wind loading. Proceedings of a Conference on Buildings and Structures , 54–83.

Ding, X., Chian, S.C., Lian, J., Cao, G., Shen, J., Luan, L., 2023. Wind-wave combined effect on dynamic response of soil-monopile-OWT system considering cyclic hydro-mechanical clay behavior. Computers and Geotechnics 154, 105124. doi:10.1016/j.compgeo.2022.105124.

Drennan, W.M., 2003. On the wave age dependence of wind stress over pure wind seas. Journal of Geophysical Research 108. doi:10.1029/2000jc000715.

Elsayed, M.A., 2006. Wavelet bicoherence analysis of wind–wave interaction. Ocean Engineering 33, 458–470. doi:10.1016/j.oceaneng.2005.04.013.

Ferčák, O., Bossuyt, J., Ali, N., Cal, R.B., 2022. Decoupling wind–wave–wake interactions in a fixed-bottom offshore wind turbine. Applied Energy 309, 118358. doi:10.1016/j.apenergy.2021.118358.

Feyzollahzadeh, M., Mahmoodi, M., Yadavar-Nikravesh, S., Jamali, J., 2016. Wind load response of offshore wind turbine towers with fixed monopile platform. Journal of Wind Engineering and Industrial Aerodynamics 158, 122–138. doi:10.1016/j.jweia.2016.09.007.

Goda, Y., 1999. A comparative review on the functional forms of directional wave spectrum. Coastal Engineering Journal 41, 1–20. doi:10.1142/s0578563499000024.

Group, T.W., 1988. The WAM model—a third generation ocean wave prediction model. Journal of Physical Oceanography 18, 1775–1810. doi:10.1175/1520-0485(1988)018<1775:twmtgo>2.0.co;2.

Hansen, A.D., Sørensen, P., Blaabjerg, F., Becho, J., 2002. Dynamic modelling of wind farm grid interaction. Wind Engineering 26, 191–210. doi:10.1260/030952402321039403.

Hao, H., Oliveira, C., Penzien, J., 1989. Multiple-station ground motion processing and simulation based on smart-1 array data. Nuclear Engineering and Design 111, 293–310. doi:10.1016/0029-5493(89)90241-0.

He, J., 2020. Coherence and cross-spectral density matrix analysis of random wind and wave in deep water. Ocean Engineering 197, 106930. doi:10.1016/j.oceaneng.2020.106930.

He, Y., Chan, P., Li, Q., 2013. Wind characteristics over different terrains. Journal of Wind Engineering and Industrial Aerodynamics 120, 51–69. doi:10.1016/j.jweia.2013.06.016.

Højstrup, J., 1999. Spectral coherence in wind turbine wakes. Journal of Wind Engineering and Industrial Aerodynamics 80, 137–146. doi:10.1016/s0167-6105(98)00198-6.

Ji, C.Y., Zhu, L.B., Zhu, Z.S., 2011. Load analysis of 2.5mw offshore wind turbine tower. Applied Mechanics and Materials 121-126, 206–212. doi:10.4028/www.scientific.net/amm.121-126.206.

Johnson, H.K., Højstrup, J., Vested, H.J., Larsen, S.E., 1998. On the dependence of sea surface roughness on wind waves. Journal of Physical Oceanography 28, 1702–1716. doi:10.1175/1520-0485(1998)028<1702:otdoss>2.0.co;2.

Jonkman, J., 2010. Definition of the Floating System for Phase IV of OC3. Technical Report. doi:10.2172/979456.

Jonkman, J.M., 2007. Dynamics Modeling and Loads Analysis of an Offshore Floating Wind Turbine. Technical Report. doi:10.2172/921803.

Karimirad, M., Moan, T., 2012. Wave- and wind-induced dynamic response of a spar-type offshore wind turbine. Journal of Waterway, Port, Coastal, and Ocean Engineering 138, 9–20. doi:10.1061/(asce)ww.1943-5460.0000087.

Kudryavtsev, V.N., Makin, V.K., Chapron, B., 1999. Coupled sea surface-atmosphere model: 2. spectrum of short wind waves. Journal of Geophysical Research: Oceans 104, 7625–7639. doi:10.1029/1999jc900005.

Li, X., Zhang, W., 2020. Long-term assessment of a floating offshore wind turbine under environmental conditions with multivariate dependence structures. Renewable Energy 147, 764–775. doi:10.1016/j.renene.2019.09.076.

Lian, J., Zhao, Y., Dong, X., Lian, C., Wang, H., 2021. An experimental investigation on long-term performance of the wide-shallow bucket foundation model for offshore wind turbine in saturated sand. Ocean Engineering 228, 108921. doi:10.1016/j.oceaneng.2021.108921.

Liu, F., Gao, S., Han, H., Tian, Z., Liu, P., 2019. Interference reduction of high-energy noise for modal parameter identification of offshore wind turbines based on iterative signal extraction. Ocean Engineering 183, 372–383. doi:10.1016/j.oceaneng.2019.05.009.

Matha, D., 2010. Model Development and Loads Analysis of an Offshore Wind Turbine on a Tension Leg Platform with a Comparison to Other Floating Turbine Concepts: April 2009. Technical Report. doi:10.2172/973961.

Moriarty, P.J., Hansen, A.C., 2005. AeroDyn Theory Manual. Technical Report. doi:10.2172/15014831.

Murtagh, P., Basu, B., Broderick, B., 2005. Along-wind response of a wind turbine tower with blade coupling subjected to rotationally sampled wind loading. Engineering Structures 27, 1209–1219. doi:10.1016/j.engstruct.2005.03.004.

Murtagh, P.J., Basu, B., Broderick, B.M., 2004. Mode acceleration approach for rotating wind turbine blades. Proceedings of the Institution of Mechanical Engineers, Part K: Journal of Multi-body Dynamics 218, 159–167. doi:10.1243/1464419042035962.

Pettersson, H., 2003. Directional wave measurements from three wave sensors during the FETCH experiment. Journal of Geophysical Research 108. doi:10.1029/2001jc001164.

Shinozuka, M., Deodatis, G., 1991. Simulation of stochastic processes by spectral representation. Applied Mechanics Reviews 44, 191–204. doi:10.1115/1.3119501.

Simiu, E., 1974. Wind spectra and dynamic alongwind response. Journal of the Structural Division 100, 1897–1910. doi:10.1061/jsdeag.0003880.

Sørensen, P., Hansen, A.D., Rosas, P.A.C., 2002. Wind models for simulation of power fluctuations from wind farms. Journal of Wind Engineering and Industrial Aerodynamics 90, 1381–1402. doi:10.1016/s0167-6105(02)00260-x.

Ti, Z., Zhou, Y., 2022. Frequency domain modeling of long-span sea-crossing bridge under stochastic wind and waves. Ocean Engineering 255, 111425. doi:10.1016/j.oceaneng.2022.111425.

Tian, D., He, W., Wang, N.B., 2012. Effect of coherence function on rotational fourier spectrum of wind turbine. Advanced Materials Research 608-609, 506–512. doi:10.4028/www.scientific.net/amr.608-609.506.

Vigueras-Rodríguez, A., Sørensen, P., Viedma, A., Donovan, M., Lázaro, E.G., 2012. Spectral coherence model for power fluctuations in a wind farm. Journal of Wind Engineering and Industrial Aerodynamics 102, 14–21. doi:10.1016/j.jweia.2011.12.006.

Wu, J., 1969. Reply [to "comment on paper by j. wu, 'wind stress and surface roughness at air-sea interface'"]. Journal of Geophysical Research 74, 5563–5563. doi:10.1029/jc074i023p05563.

Zhang, Z., Staino, A., Basu, B., Nielsen, S.R., 2016. Performance evaluation of full-scale tuned liquid dampers (TLDs) for vibration control of large wind turbines using real-time hybrid testing. Engineering Structures 126, 417–431. doi:10.1016/j.engstruct.2016.07.008.

Zountouridou, E., Kiokes, G., Chakalis, S., Georgilakis, P., Hatziargyriou, N., 2015. Offshore floating wind parks in the deep waters of mediterranean sea. Renewable and Sustainable Energy Reviews 51, 433–448. doi:10.1016/j.rser.2015.06.027.